EES Catalysis

PAPER

View Article Online
View Journal | View Issue

Cite this: *EES Catal.*, 2024, 2, 953

Probing the active sites of oxide encapsulated electrocatalysts with controllable oxygen evolution selectivity†

William D. H. Stinson,[a] Robert S. Stinson,[a] Jingjing Jin,[a] Zejie Chen,[b] Mingjie Xu,[c] Fikret Aydin,[d] Yinxian Wang,[a] Marcos F. Calegari Andrade,[d] Xiaoqing Pan,[cef] Tuan Anh Pham,[d] Katherine E. Hurst,[g] Tadashi Ogitsu,[d] Shane Ardo[beh] and Daniel V. Esposito*[a]

Electrocatalysts encapsulated by nanoscopic overlayers can control the rate of redox reactions at the outer surface of the overlayer or at the buried interface between the overlayer and the active catalyst, leading to complex behavior in the presence of two competing electrochemical reactions. This study investigated oxide encapsulated electrocatalysts (OECs) comprised of iridium (Ir) thin films coated with an ultrathin (2–10 nm thick) silicon oxide (SiO_x) or titanium oxide (TiO_x) overlayer. The performance of SiO_x|Ir and TiO_x|Ir thin film electrodes towards the oxygen evolution reaction (OER) and Fe(II)/Fe(III) redox reactions were evaluated. An improvement in selectivity towards the OER was observed for all OECs. Overlayer properties, namely ionic and electronic conductivity, were assessed using a combination of electroanalytical methods and molecular dynamics simulations. SiO_x and TiO_x overlayers were found to be permeable to H_2O and O_2 such that the OER can occur at the MO_x|Ir (M = Ti, Si) buried interface, which was further supported with molecular dynamics simulations of model SiO_2 coatings. In contrast, Fe(II)/Fe(III) redox reactions occur to the same degree with TiO_x overlayers having thicknesses less than 4 nm as bare electrocatalyst, while SiO_x overlayers inhibit redox reactions at all thicknesses. This observation is attributed to differences in electronic transport between the buried interface and outer overlayer surface, as measured with through-plane conductivity measurements of wetted overlayer materials. These findings reveal the influence of oxide overlayer properties on the activity and selectivity of OECs and suggest opportunities to tune these properties for a wide range of electrochemical reactions.

Received 8th April 2024,
Accepted 15th April 2024

DOI: 10.1039/d4ey00074a

rsc.li/eescatalysis

Broader context

The need for high performance electrocatalysts represents a significant barrier to the widespread implementation of renewable energy technologies like electrolyzers, fuel cells, and photocatalytic reactors. These electrocatalysts will typically need to be highly selective towards formation of the product(s) of interest, withstand thousands of hours of operation, and be capable of operating at high current densities with minimal kinetic losses. Towards this end, encapsulating active electrocatalysts with semi-permeable, nanoscopic oxide overlayers is a promising approach to modulate the local microenvironment of conventional electrocatalyst materials in ways that inhibit degradation mechanisms, improve catalytic activity, and/or enhance redox selectivity. Using silicon and titanium oxide nanocoatings as a case study, the current study explains how the electrical and species transport properties of oxide overlayers coated on state-of-the-art iridium oxygen evolution electrocatalysts strongly influences the rates of reactions occurring on the outer surface of the overlayer relative to reactions at the overlayer/catalyst buried interface.

[a] *Department of Chemical Engineering, Columbia Electrochemical Engineering Center, Lenfest Center for Sustainable Energy Columbia University in the City of New York, New York, NY 10027, USA. E-mail: de2300@columbia.edu*
[b] *Department of Chemistry, University of California, Irvine, California 92697, USA*
[c] *Irvine Materials Research Institute (IMRI), University of California, Irvine, 92697, USA*
[d] *Materials Science Division, Lawrence Livermore National Laboratory, Livermore, California 94550, USA*
[e] *Department of Materials Science and Engineering, University of California, Irvine, California 92697, USA*
[f] *Department of Physics and Astronomy, University of California, Irvine, California 92697, USA*
[g] *Energy Conversion and Storage Systems Center National Renewable Energy Laboratory, Golden, CO 80401, USA*
[h] *Department of Chemistry and Biomolecular Engineering, University of California, Irvine, California 92697, USA*

† Electronic supplementary information (ESI) available. See DOI: https://doi.org/10.1039/d4ey00074a

I. Introduction

The need for high performance electrocatalysts represents a significant barrier to the widespread implementation of renewable energy technologies.[1] One promising approach to improve electrocatalyst performance is to encapsulate the active catalyst with a semi-permeable oxide overlayer.[2] Such oxide encapsulated electrocatalysts (OECs) offer several potential advantages over traditional electrocatalysts, including increased stability,[3–5] tolerance to catalyst poisons,[6] improved activity,[7,8] and enhanced selectivity.[9–12] Studies of encapsulated electrocatalysts based on chromium oxide (CrO_x),[10] manganese oxide (MnO_x),[13] and silicon oxide (SiO_x)[6,11] have provided evidence that the overlayers can act as ionically-conducting, electronically-insulating coatings that permit reactant/product species transport between the bulk electrolyte and active sites at the buried interface between the overlayer and catalyst. In contrast, several studies on titanium dioxide (TiO_x) overlayers have indicated that the overlayer itself can facilitate electron transfer to/from its outer surface where active sites catalyze reactions of interest.[14–16] Various explanations for improved activity or selectivity of OECs have been proposed, including the ability of overlayers to facilitate selective species transport and/or electronic interactions between the overlayer and electrocatalyst that enhance activity.[14,17,18] A deeper understanding of how ionic and electronic conductivities can affect the activity and selectivity of oxide overlayers is needed to inform rational design of OECs.

In this work, the primary interest is the design of OECs for selectively promoting the oxygen evolution reaction (OER) in the presence of a competing redox reaction that is thermodynamically favored over the OER. The OER, shown below for acidic electrolytes, is of practical importance to a wide range of electrolytic processes.[19]

$$2H_2O \rightarrow O_2 + 4H^+ + 4e^- \quad E^\circ = 1.23\ \text{V } \textit{vs.}\ \text{RHE} \qquad (1)$$

The oxide encapsulated architecture has attracted significant interest for improving OER electrocatalyst stability, activity, and selectivity in the presence of competing oxidation reactions.[8,11,13,20] However, explanations of the mechanistic details of how oxide overlayers enhance the performance of OER electrocatalysts can vary greatly among studies. In their investigations of TiO_2-encapsulated iridium and ruthenium electrocatalysts, Finke *et al.* indicated that the OER occurs at the outer surface of the TiO_2 overlayers and attributed increases in OER activity to electronic interactions between the IrO_x and TiO_2 layers.[14] This reaction scheme requires that the outer surface of the overlayer be catalytically active for the reaction of interest and that facile electron transport occurs between the active sites and the underlying catalyst or support material, as illustrated in Fig. 1a. In contrast, other studies of OECs based on SiO_x,[6,11] MnO_x[13] and CeO_x[21] encapsulated OER catalysts have hypothesized that the OER occurs predominantly at the buried interface between the overlayer and active electrocatalyst. As illustrated in Fig. 1b, such a reaction scheme requires transport of reactants and products (H_2O, OH^-, H^+, and O_2 for the OER) through the overlayer while inferring that poor electronic conductivity and/or catalytic activity of the overlayer limits reactions from occurring at the outer surface. Collectively, recent studies of OECs for the OER have demonstrated the promise of this electrocatalyst architecture to improve OER electrocatalyst performance but also highlight the lack of a comprehensive understanding for how overlayer ionic and electronic conductivity can influence the location of active sites for competing reactions, and thus the overall electrode performance.

In this study, planar thin film electrodes such as those shown in Fig. 1c and e are used, whereupon SiO_x and TiO_x overlayers were deposited by photochemical deposition.[22] Such thin film electrodes are more conducive to measuring the electronic and ionic transport properties of oxide overlayers.

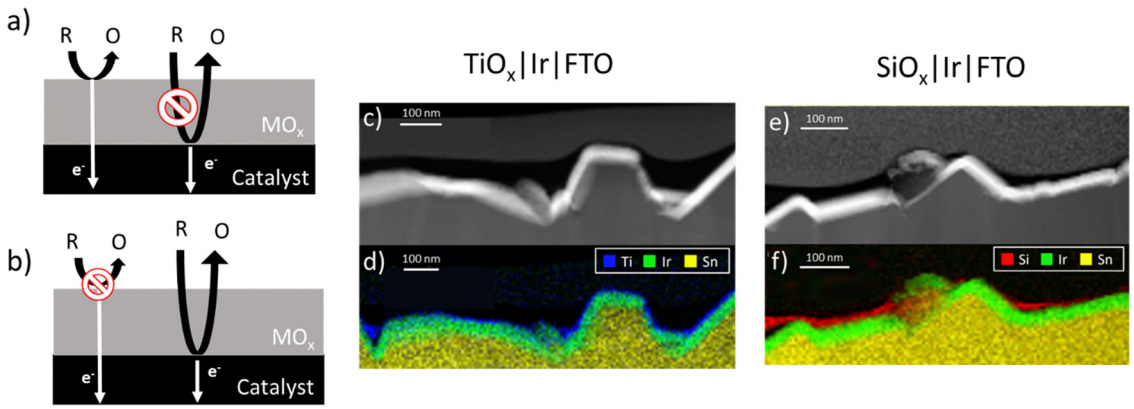

Fig. 1 Schematic side-views of oxide encapsulated electrocatalysts (OECs) for which the oxide overlayer (a) possesses sufficient electronic conductivity, active site density and activity so that redox reactions on the outer surface of the oxide overlayer occur more rapidly than species transport and subsequent redox reactivity at the overlayer-catalyst buried interface, or (b) possesses insufficient electronic conductivity, active site density, or activity on the outer surface in comparison to the rate of species transport and subsequent redox reactivity at active sites in the buried interface. (c) and (e) dark field cross-sectional scanning transmission electron microscopy (STEM) images of TiO_x|Ir and SiO_x|Ir electrodes, respectively. (d) and (f) corresponding elemental maps of TiO_x|Ir and SiO_x|Ir electrodes, respectively, measured by STEM/EDS (yellow: Sn, green: Ir, red: Si, and blue: Ti).

As an additional probe reaction, the aqueous ferric/ferrous redox couple (eqn (2)) was investigated:

$$Fe^{2+}(aq) \rightarrow Fe^{3+}(aq) + e^{-} \quad E^{\circ} = 0.771 \text{ V } vs. \text{ NHE} \qquad (2)$$

The ferric and ferrous ions exist as both aquo- and sulfate complexes,[23] but will be referred in this article as Fe(III) and Fe(II) for simplicity. Unlike the OER, this reaction involves only a single electron transfer and is known to exhibit facile kinetics for a variety of electrode materials ranging from Pt group metals[24] to carbon.[25] Due to its formal reduction potential being located in between those for H^+/H_2 and $H_2O/O_2,H^+$, this reaction is also of practical interest as a redox mediator for use in photocatalytic Z-scheme water splitting.[26,27] Owing to the relatively fast kinetics for the Fe(II)/Fe(III) reaction on many conductive materials, it is plausible that OECs containing overlayers possessing sufficiently high electronic conductivity can carry out the Fe(II) oxidation reaction on the outer surface of the overlayer as shown in Fig. 1a. In contrast, OECs with overlayers that are electronically insulating and significantly impermeable to Fe(II) are not expected to display any significant activity towards Fe(II) oxidation.

In the present study, it is demonstrated that Ir electrodes possessing TiO_x or SiO_x overlayers with thickness >10 nm can significantly enhance selectivity towards the OER reaction. Furthermore, we show that TiO_x overlayers can have sufficient electronic conductivity to facilitate Fe(II) oxidation at the outer surface of the overlayer, although the reaction rate may be limited by the availability of active sites. In contrast, SiO_x overlayers are found to be both electronically resistive and electrochemically inert with low permeability for the Fe(II)/Fe(III) redox couple, allowing for higher OER selectivity compared to TiO_x-encapsulated Ir electrodes having similar overlayer thickness.

II. Results and discussion

2.1. Electrode characterization

Full details of electrode fabrication and characterization procedures are provided in the Materials and methods section. Briefly, iridium (Ir) thin film electrodes were fabricated using physical vapor deposition to deposit ≈ 50 nm of Ir onto fluorine doped tin oxide (FTO)-coated glass substrates. Next, TiO_x or SiO_x overlayers were deposited by a low-temperature photochemical conversion process[22,28] using three concentrations of precursors (low, medium, high) to create TiO_x|Ir and SiO_x|Ir electrodes. The low, medium, and high solution concentrations yielded oxide layer thicknesses of ≈ 2, 5 and 10 nm, respectively, when oxide overlayers were deposited on separate smooth platinum-coated Si wafers and measured using ellipsometry. However, overlayer thicknesses could not be determined using the same method on the rougher FTO substrates, for which reason oxide encapsulated electrodes deposited on FTO/glass substrates will henceforth be referred to by their solution concentration rather than overlayer thickness.

Fig. 1c and e show representative cross-section STEM images of high concentration TiO_x|Ir and SiO_x|Ir electrodes with corresponding energy dispersive X-ray spectroscopy (EDS) maps of identical areas of these electrodes displayed in Fig. 1d and f. Despite the notable roughness of the Ir thin films that results from the underlying FTO layer, the low-resolution images show thin TiO_x and SiO_x overlayers stretching across the field of view in all images taken. However, the thickness of the oxide overlayers is non-uniform, appearing to be thickest in the cavities of the FTO substrate and thinnest on the high points. This observation from cross-sectional STEM images was further confirmed by atomic force microscopy (AFM) images measured before and after deposition of the oxide coatings (Fig. S1, ESI†). While the root mean squared (rms) roughness of the Ir|FTO substrate was found to be 38 nm, deposition of the oxide overlayers consistently resulted in a decrease in the root-mean-square roughness by 7–18% (Supporting Section SI, ESI†). STEM bright-field/EDS line scans measured perpendicular to the overlayer/Ir buried interface (Fig. 2b and d) suggest there could be some intermixing between the overlayers and iridium, but the lack of a sharp MO_x|Ir (M = Ti, Si) interface may also result from the roughness of the FTO substrate, which is evident from low-resolution images (Fig. S2, ESI†). Overlayer thicknesses ranging between 10–15 nm were determined for both the TiO_x|Ir and SiO_x|Ir electrodes from additional STEM/EDS line scans (Fig. S3–S6, ESI†). High resolution STEM bright-field images of the high concentration TiO_x|Ir (Fig. 2a) and SiO_x|Ir (Fig. 2c) electrodes suggest that both types of overlayers are amorphous, which is further supported by analysis of the electron diffraction patterns using the bandpass method in DigitalMicrograph (Fig. S7, ESI†).

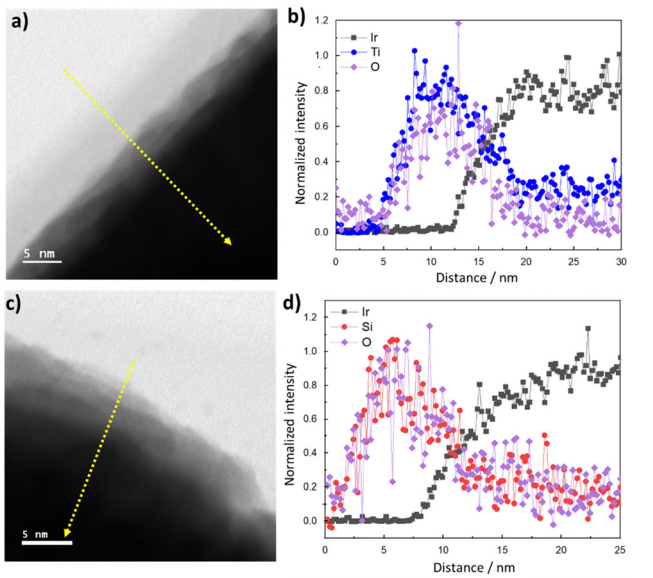

Fig. 2 STEM bright-field images of (a) high precursor concentration TiO_x|Ir and (c) SiO_x|Ir electrodes alongside (b) and (d) normalized EDS elemental line scan profiles corresponding to the locations of the dashed yellow lines in (a) and (c).

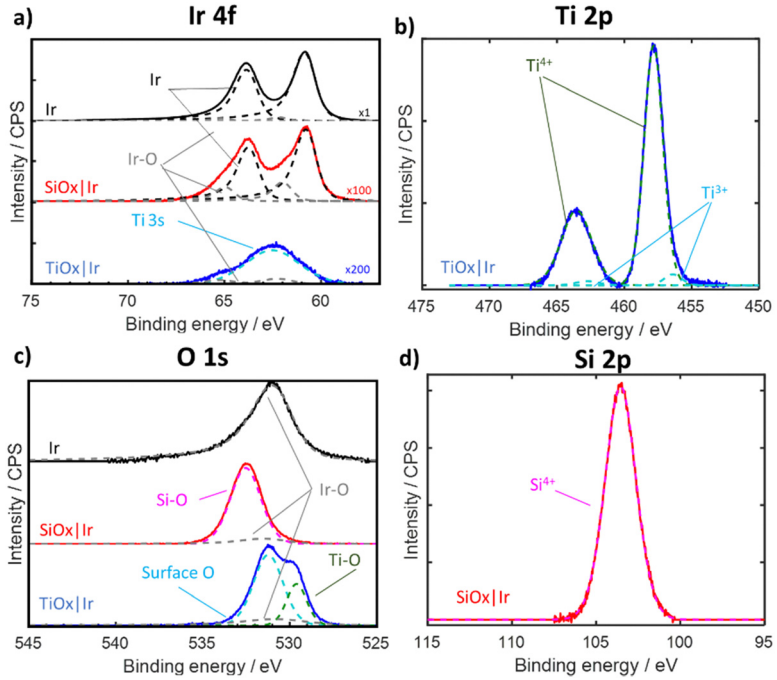

Fig. 3 XPS spectra of bare Ir (black trace), "high" SiO_x|Ir (red trace) and "high" TiO_x|Ir (blue trace) electrodes. (a) Ir 4f, (b) Ti 2p, (c) O 1s and (d) Si 2p regions. Dashed lines in all XPS regions correspond to fitted spectra with labels indicating the type of bond or oxidation state. Ir 4f region was scaled by 100× and 200× for SiO_x|Ir and TiO_x|Ir, respectively, for visualization. Details related to peak fitting are found in Supporting Section SIII (ESI†).

Overlayers deposited using the lower concentration MO_x|Ir electrodes could not be directly visualized *via* EDS/STEM due to the small amount of overlayer material and the rough Ir|FTO substrate (Fig. S8–S11, ESI†). XPS measurements of the "low" and "medium" samples are consistent with high coverages of the oxide layers (Fig. S14, ESI†), although it is also possible that thinnest overlayers made from the low and medium precursor concentrations are semi-continuous with breaks in the overlayers corresponding to the high points or peaks in the Ir substrate. Such morphology was previously seen for silicon oxide nanolayers deposited by the same method onto platinum particles.[5]

Electrodes were also characterized by X-ray photoelectron spectroscopy (XPS), with Ir 4f, Si 2p, Ti 2p, and O 1s spectra shown in Fig. 3 for electrodes containing overlayers made with the highest precursor concentration. Full details on acquisition and peak fitting analysis, as well as XPS of the lower precursor samples, can be found in the Supporting Section SIII (Fig. S12–S14, ESI†). The Ir 4f region (Fig. 3a) of bare Ir and SiO_x|Ir electrodes displays peaks corresponding to both metallic Ir and IrO_x with Ir 4f 7/2 peak locations within 0.1 eV of the literature value (60.8 eV for Ir, and 61.6 eV for IrO_2).[29] The Ir 4f region for the TiO_x|Ir electrode includes Ti 3s signal from the TiO_x overlayer that overlaps with the Ir 4f signal, yielding less-defined Ir 4f peaks.[30–32] Both SiO_x|Ir and TiO_x|Ir electrodes show significantly lower Ir 4f signal compared to bare Ir due to screening by the overlayer. The ratio of Ir 4f peak areas associated with IrO_x and Ir increased to a value of 0.3 for SiO_x|Ir compared to a value of 0.05 for non-treated bare Ir, which may be explained by partial oxidation of Ir caused by the UV-Ozone curing process. This was confirmed by carrying out XPS on a second bare Ir electrode that underwent the same UV-Ozone treatment (Fig. S12, ESI†), which showed a IrO_x : Ir peak area ratio of 0.2 which was similar to that of the SiO_x|Ir sample.

The O 1s region (Fig. 3c) for bare Ir displays an asymmetric peak centered at 530.9 eV that corresponds to a mixture of Ir-oxide species.[29] This O 1s peak associated with IrO_x species was also evident in the TiO_x|Ir and SiO_x|Ir electrodes but was greatly diminished due to screening from the overlayer. Two additional O 1s peaks are present for the TiO_x|Ir electrode, whereas only one other O 1s peak is found for the SiO_x|Ir electrode. The two additional O 1s peaks for the TiO_x|Ir electrode centered at 529.6 eV and 531.2 eV can be attributed to oxygen in the TiO_x lattice (*e.g.* Ti–O–Ti) and surface oxygen (seen as Ti–OH or adsorbed H_2O), respectively.[33,34] Fitting the Ti 2p region (Fig. 3b) reveals a large doublet associated with Ti^{4+} (from TiO_2) and a minor doublet associated with the more reduced Ti^{3+} (either from Ti–OH or Ti neighboring oxygen vacancies).[14,33] Meanwhile, the pronounced O 1s peak centered at 532.5 eV for the SiO_x|Ir electrode can be attributed to oxygen in SiO_2[35] (Fig. 3c), while a single peak seen in the Si 2p region is consistent with Si^{4+} in SiO_2 (Fig. 3d).

2.2. Electrochemical performance of OECs towards OER and Fe(II) oxidation

To assess the electrochemical performance of oxide encapsulated Ir electrodes towards the OER, cyclic voltammetry (CV) measurements on bare Ir, SiO_x|Ir, and TiO_x|Ir electrodes were performed in deaerated aqueous 0.1 M Na_2SO_4 + 0.05 M H_2SO_4 with the pH adjusted to 1.5. CVs for bare Ir, high precursor

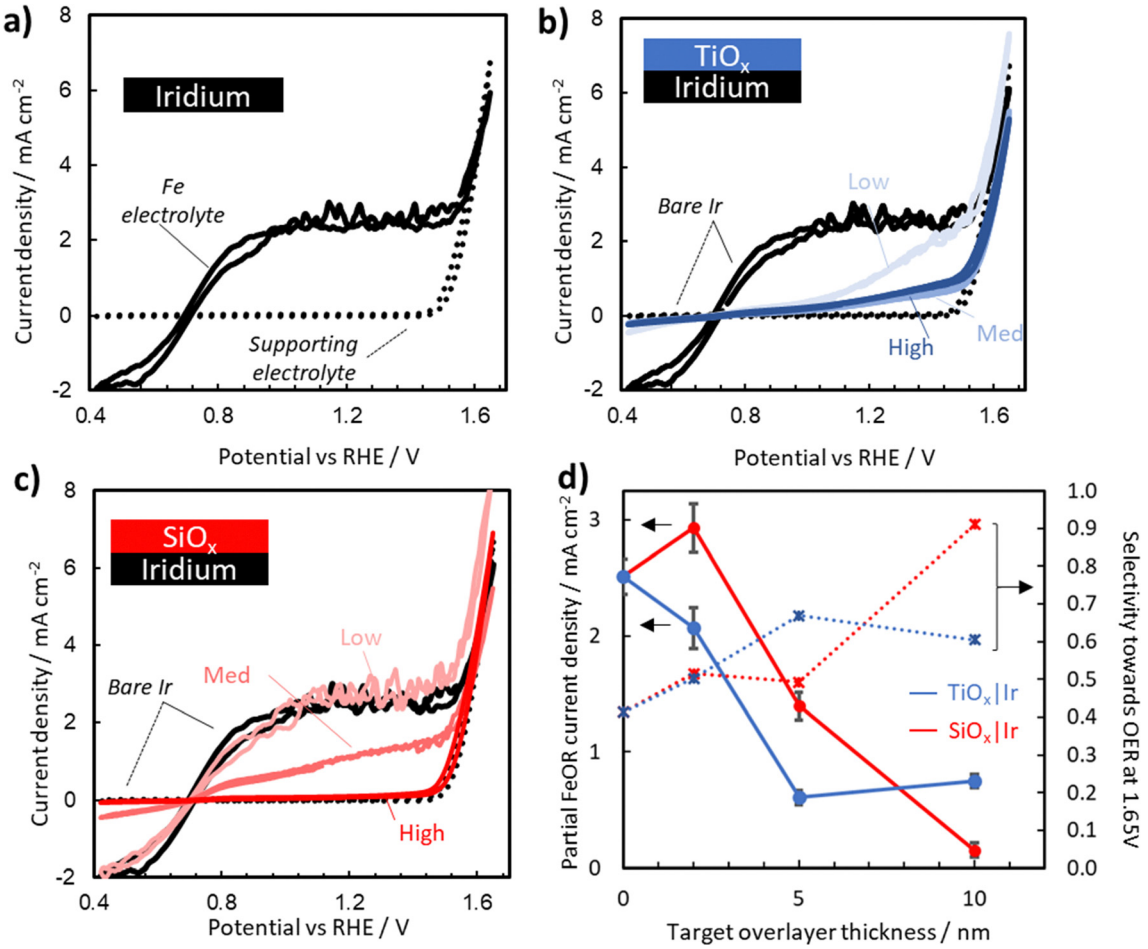

Fig. 4 Representative CV curves recorded for (a) bare Ir electrodes in deaerated aqueous 0.1 M Na_2SO_4 + 0.05 M H_2SO_4 (pH adjusted to 1.5) supporting electrolyte (dotted line) and an Fe-containing electrolyte with additional 25 mM $FeSO_4$ and 12.5 mM $Fe_2(SO_4)_3$ (solid line). CV curves recorded in the Fe-containing electrolyte for (b) TiO_x|Ir and (c) SiO_x|Ir electrodes made with three different precursor concentrations. Supporting electrolyte scans (dotted) for the high concentration MO_x|Ir (M = Ti, Si) electrode and scans in the Fe-containing electrolyte for the bare Ir (solid black curves) are added for reference. (d) Partial Fe(II) oxidation current density taken at 1.45 V *vs.* RHE (solid) and selectivity towards the OER taken at 1.65 V *vs.* RHE (dotted) for each of the electrodes plotted as a function of targeted overlayer thickness, where the red and blue data points correspond to SiO_x|Ir and TiO_x|Ir electrodes, respectively. Error bars indicate standard deviation in the current density taken on the final CV over a 10 mV window around 1.45 V *vs.* RHE for both the forward and reverse scan. CV curves for bare Ir and high concentration SiO_x|Ir are reproduced from ref. 40.

concentration TiO_x|Ir, and high precursor concentration SiO_x|Ir are provided as dotted curves in Fig. 4a–c. Additional CVs for the other oxide precursor concentrations can be found in Fig. S15 (ESI†). The only significant feature observed for all electrodes in the supporting electrolyte is the oxidation current associated with the OER. Consistent with previously reported results for Ir-based OER electrocatalysts,[36–39] all of these electrodes exhibit OER onset potentials around 1.55 V *vs.* RHE, and Tafel slopes of 48–61 mV dec^{-1} (Fig. S17 and Table S2, ESI†). When the CV curves for the bare Ir, TiO_x|Ir, and SiO_x|Ir electrodes are overlaid (Fig. S15, ESI†), a minor increase in OER activity can be seen for the SiO_x|Ir electrodes while a decrease in activity is seen for TiO_x|Ir electrodes. Comparison with a bare Ir electrode subjected to the same UV-ozone treatment as the coated electrodes (Fig. S15, ESI†) shows a similar improvement in activity, but was not consistent across multiple samples (Fig. S16, ESI†) suggesting differences can most likely be attributed to the influence of the oxide coating rather than changes to the buried Ir catalyst caused by the UV-ozone treatment. Importantly, the presence of thin (< 15 nm) SiO_x and TiO_x overlayers only alter the OER overpotential by $<$ 10 mV and < 35 mV, respectively, at 4 mA cm^{-2} as compared to the uncoated UV-ozone Ir (Fig. S15 and Table S1, ESI†).

To assess stability of MO_x overlayers during extended OER operating conditions, chronoamperometric (CA) scans were recorded at 1.65 V *vs.* RHE for 10 hours in 50 mM H_2SO_4 + 500 mM Na_2SO_4 (Fig. S18a, ESI†) for both high concentration MO_x|Ir electrodes and a bare Ir control. All three thin film electrodes displayed gradual decreases in current density over the course of the 10 hour measurement and similar final current densities. Post-CA XPS characterization of the spent electrodes (Fig. S18c and d, ESI†) revealed that the TiO_x overlayer was no longer present, while the magnitude of the Si 2p signal associated with the SiO_x overlayer had decreased by 35%.

More investigations are needed to understand and deconvolute the activity and stability changes under longer duration operation. However, for the current study, measurements were limited to short duration (< 60 min of electrochemical measurements) to focus on establishing the structure–property–performance relationships of as-made MO_x|Ir electrodes.

Fig. 4a–c also contain CV curves (solid lines) recorded in the presence of 25 mM $FeSO_4$ and 12.5 mM $Fe_2(SO_4)_3$ for MO_x|Ir with three different overlayer precursor concentrations. The partial current associated with the Fe(II)/Fe(III) electrochemistry can be estimated by the difference between the CV curves containing Fe(II)/Fe(III) (solid lines) and those in the Fe-free supporting electrolyte (dotted lines). For bare Ir (Fig. 4a), pronounced Fe(II) oxidation (FeOR) and Fe(III) reduction (FeRR) signal is observed with sharp increases in current density on either side of the Fe(II)/Fe(III) formal reduction potential ($E'_{Fe(II)/Fe(III)}$) of 0.77 V *vs.* RHE, reflecting the facile reaction kinetics for the Fe(II)/Fe(III) reaction on bare Ir. At overpotentials larger than ± 0.3 V *vs.* $E'_{Fe(II)/Fe(III)}$, the FeRR and the FeOR current densities level off and reach a limiting current density of ≈ 3.0 mA cm^{-2} associated with mass transfer of Fe(III)/Fe(II) across the diffusion boundary layer. Scanning to even larger overpotentials, the oxidation current rapidly increases at ≈ 1.55 V *vs.* RHE. This closely matches the OER onset potential observed in the supporting electrolyte, strongly suggesting that the increase in oxidation current in the Fe-containing electrolyte beyond 1.55 V *vs.* RHE is also associated with the OER.

Interestingly, the magnitude of the FeOR current observed between 0.77 V and 1.55 V *vs.* RHE varies greatly between the bare Ir and MO_x|Ir electrodes. For SiO_x|Ir electrodes, the FeOR current decreases monotonically from 3.0 mA cm^{-2} at a potential of 1.45 V *vs.* RHE for the ''low'' electrode containing the thinnest overlayer down to only ≈ 0.25 mA cm^{-2} for the ''high'' electrode with the thickest overlayer (Fig. 4d). The presence of TiO_x overlayers also decreases the FeOR relative to bare Ir, but only to ≈ 0.5 mA cm^{-2} at 1.45 V *vs.* RHE for the highest overlayer concentration. Additionally, the decrease in FeOR does not follow the same monotonic trend as with SiO_x, nor do they reach a constant mass-transport-limited current density for Fe(II) oxidation before the OER onset potential.

Selectivities of each electrode towards the OER (S_{O2}) over the FeOR were estimated by linear extrapolation of the FeOR current to potentials above 1.45 V *vs.* RHE as described in the Section SVII (Fig. S19, ESI†), and are provided in Fig. 4d as a function of MO_x (M = Ti, Si) overlayer thickness. While a minor decrease in OER activity was seen for all electrodes when scanned in Fe electrolyte (Table S1, ESI†), MO_x|Ir electrodes had a reduced impact on OER in Fe containing electrolyte. For example, at 4 mA cm^{-2}, there was an additional overpotential of 68 mV required for bare Ir, while the high concentration SiO_x and TiO_x only needed additional overpotentials of 20 mV and 47 mV, respectively. Both SiO_x|Ir and TiO_x|Ir electrodes achieve enhanced selectivity towards the OER compared to bare Ir. At 1.65 V *vs.* RHE, S_{O2} values of 40%, 60%, and 91% were determined for the bare Ir, thick TiO_x|Ir and thick SiO_x|Ir electrodes, respectively.

These results demonstrate the ability to alter oxide overlayer thickness to manipulate the current density of a competing reaction (FeOR) while leaving the desired reaction (OER) minimally affected compared to bare Ir. This is a remarkable result given the thermodynamic and kinetic advantages of the FeOR over the OER. Such behavior is desirable for a wide range of applications, such as Z-scheme water splitting by photocatalysis, where the presence of undesired competing reactions can drastically reduce system efficiency.[41,42] However, it is not clear from the results of Fig. 4 what the physical origin of the enhanced OER selectivity is, and where the active sites for OER and Fe(II) oxidation are located within these composite electrodes. To better address these questions and identify which scenarios from Fig. 1 are most likely responsible for the enhanced selectivity of oxide encapsulated electrodes, experiments and simulations were carried out to assess the ability of SiO_x and TiO_x overlayers to facilitate electrocatalytic reactions, electron transport, and ion transport.

2.3. Electronic conductivity of oxide overlayers

To assess the electronic conductivity of TiO_x and SiO_x overlayers in contact with the electrolyte, a set of electrodes were fabricated with a thin (≈ 1 nm) layer of Pt deposited on top of SiO_x|Pt|p + Si(100) and TiO_x|Pt|p + Si(100) electrodes to create a ''sandwich structure'' as illustrated in Fig. 5a. The thin outer Pt layer introduces catalytic sites on the outer surface of the oxide overlayer where Fe(II)/Fe(III) redox reactions can occur. The use of a very thin Pt layer helps to minimize any influence of electrical shunts between the inner and outer Pt layers as a high sheet resistance limits lateral charge transport. Thus, the electrochemical current recorded for such sandwich structure electrodes must involve electron transfer across the oxide layer, which can become rate limiting for thicker, resistive overlayers at overpotentials for which reaction kinetics are fast. Under these conditions, the electronic resistivity of the thin oxide layers can be estimated within the electrochemical environment of interest.[43]

The electronic conductivity of SiO_x and TiO_x sandwich structure electrodes were evaluated by carrying out CVs in the same Fe-containing electrolyte used in Section 2.2. Electrodes were mounted on a custom Teflon holder attached to a rotator to ensure consistent mass transport and completed at three different rotation rates. CV curves for Pt|TiO_x|Pt and Pt|SiO_x|Pt electrodes are provided in Fig. 5b and c, respectively, for oxide layer thicknesses varying between 1 nm and 12 nm, which were generated through varying precursor concentration and measured through ellipsometry. Focusing first on the bare Pt control electrode, symmetric CV curves are observed that switch between oxidation and reduction current at the formal reduction potential for Fe(II) and Fe(III), with clear mass transfer limiting current densities associated with Fe(II) oxidation at positive potentials and Fe(III) reduction at negative potentials. Pt|SiO_x|Pt and Pt|TiO_x|Pt electrodes show a similar profile as the CV curve for the bare Pt electrode, but generally appear to be skewed to larger overpotentials. A monotonic decrease in current density is observed with increasing thickness of the

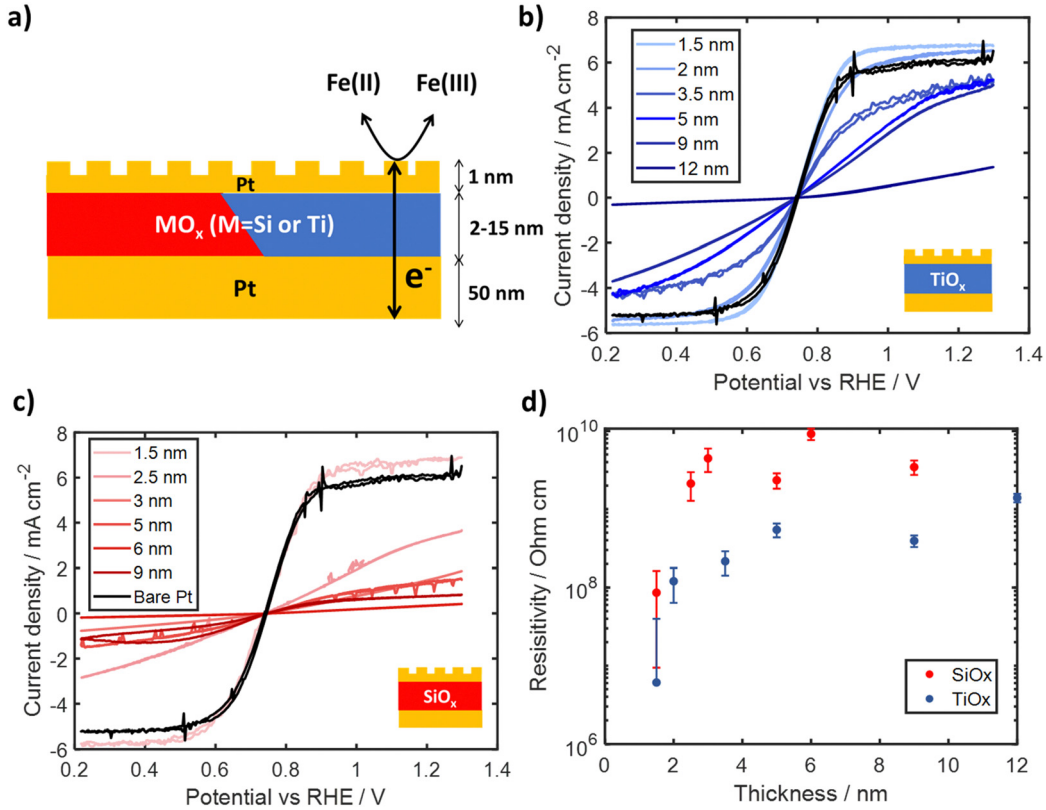

Fig. 5 (a) Schematic of "sandwich" structure electrodes used for electronic conductivity measurements. Representative CV curves recorded for (b) Pt|TiO_x|Pt and (c) Pt|SiO_x|Pt electrodes mounted onto a rotator in deaerated aqueous 25 mM $FeSO_4$ and 12.5 mM $Fe_2(SO_4)_3$ (pH adjusted to 1.5) with a scan rate of 10 mV s^{-1} for 4 cycles at an RPM of 250. Figure legends report the thickness of the oxide layer. (d) Electronic resistivities of SiO_x and TiO_x overlayers calculated from analysis of CV curves in (b) and (c), plotted as a function of overlayer thickness. Error bars in (d) are the propagated standard deviation associated with resistance and thickness measurements.

oxide interlayer. The large suppression in both the apparent FeRR and FeOR limiting current density for Pt|SiO_x|Pt electrodes can be seen for almost all thicknesses. However, these current densities seem to still have a positive slope suggesting the electrodes are likely not mass-transport limited, but electronically limited. This conclusion is supported by a Levich analysis (Fig. S23 and S24, ESI†), where the calculated Fe(II) and Fe(III) diffusion coefficients for electrodes containing oxide layers with thicknesses >3 nm are an order of magnitude lower than literature values.[44]

As all electrodes shown in Fig. 5 were tested under identical conditions and contain the same amount of Pt on their outer surface, the differences in CV curves can be attributed to ohmic overpotentials associated with the transport of electrons across the oxide layer interposed between the inner and outer Pt layers. The calculated oxide layer resistances and resistivities for each electrode are plotted in Fig. S21 and Fig. 5d (ESI†), respectively, as a function of oxide overlayer thickness at the highest rotation speed of 250 RPM. Full details on determination of resistances and resistivities are provided in Supporting Section SVIII (Fig. S20–S24, ESI†). Fig. 5d shows that the resistivity of both SiO_x and TiO_x increases with thicknesses up to 3–5 nm, beyond which resistivity becomes relatively independent of thickness. For SiO_x overlayers, the calculated resistivity increased from $8.6 \pm 7.6 \times 10^7$ Ω cm for 2 nm thickness up to $9.2 \pm 1.5 \times 10^9$ Ω cm for 9 nm thickness, with an average of $4.3 \pm 2.8 \times 10^9$ Ω cm for thicknesses above 3 nm. Fig. 5d also shows that the resistivities of TiO_x interlayers were found to be almost an order of magnitude lower than those for SiO_x for all thicknesses. Calculated resistivities ranged from $6.1 \pm 0.3 \times 10^6$ Ω cm at 2 nm thickness to $3.9 \pm 0.7 \times 10^8$ Ω cm at 9 nm thickness, with an average resistivity of $7.8 \pm 5.4 \times 10^8$ Ω cm for TiO_x thicknesses above 5 nm. While the electronic resistivity of oxide coatings can vary highly depending on the material synthesis and crystallinity,[45–51] the average resistivities for overlayers thicker than 3 nm are still orders of magnitude lower than those for bulk crystalline SiO_2[52,53] and TiO_2.[54–57]

The lower resistivity of oxide overlayers used in this study can most likely be attributed to the highly defective, amorphous nature of overlayers deposited by the low temperature photochemical deposition process (Fig. 2a and c), although it is also possible that residual carbon within the MO_x layer[58] could increase the conductivity. Previous studies have shown that oxygen deficient TiO_2, characterized by Ti^{3+} states such as those evident in the Ti 2p spectra in Fig. 3b, have lower resistivity compared to stoichiometric TiO_2.[59,60] The thickness-dependent resistivity of both types of MO_x layers for < 3 nm is likely influenced by quantum mechanical tunneling, which is known

to be an important mode of electron transport for thin dielectric layers in this thickness regime.[43,61,62] The slight dependence of resistivity on thickness for TiO_2 overlayers from 3 to 7 nm may suggest electronic conduction through a combination of tunneling and bulk conduction, as previously suggested in literature.[43,63]

Importantly, the high resistivities of thicker SiO_x overlayers support the hypothesis that redox reactions are not able to occur on the outer surface to any meaningful extent due to the inability of SiO_x to support electron transport between the substrate and active sites located on its outer surface. For example, a 5–10 nm thick SiO_x overlayer characterized by a resistivity of 10^9 Ω cm would incur an ohmic drop of ≈ 1 V to support a current density of ∼ 1 mA cm^{-2}. However, charge transport through TiO_x overlayers could still be significant at resistivities of 10^8 Ω cm, as the same conditions would only require ∼100 mV of additional ohmic resistance. This analysis demonstrates that TiO_x overlayers could support meaningful rates of electronic transport (such as those seen in Fig. 4b) to active sites on their outer surface.

2.4. Electrocatalytic activity of oxide overlayers

To further assess whether the outer surface of the oxide overlayers are catalytically active, SiO_x and TiO_x overlayers were also deposited on three different Ir-free substrates: FTO/glass, degenerately doped p-Si(100) (p+Si), and 50 nm thick Pt thin film on p+Si(100). CV curves were recorded in the identical electrolytes and using the same scan conditions and range of oxide layer thicknesses used in Section 2.2.

CV cycling of bare and oxide-encapsulated FTO substrates in Fe(II)/Fe(III)-containing electrolyte was used to assess the intrinsic catalytic activity and Fe blocking capabilities of overlayers in the absence of a good catalyst at the buried interface. As seen in both Fig. 6a and b, the bare FTO electrodes in the Fe-containing electrolyte exhibit notable oxidation and reduction current densities, which can be attributed to the FeOR and FeRR, respectively, but with significantly larger overpotentials and higher asymmetry than for bare Ir. These differences can be attributed to the poor catalytic activity of FTO.[64] The CVs recorded for SiO_x|FTO electrodes in the Fe-containing electrolyte, seen in Fig. 6a, show that even the thinnest SiO_x overlayer (made with the lowest precursor concentration) suppresses the Fe redox current while the thicker overlayers synthesized with the higher precursor concentrations nearly eliminate Fe redox current. The CV curves for the TiO_x|FTO electrodes, seen in Fig. 6b, display suppressed Fe(II) oxidation and Fe(III) reduction current at both the low and medium precursor concentrations, with curve shapes displaying asymmetry similar to the CV curve for bare FTO. The highest precursor concentration TiO_x|FTO electrode displays even lower FeOR and FeRR signal that is slightly larger than that seen for the medium and high concentration SiO_x|FTO electrodes.

To assess whether the roughness of the FTO substrates has a substantial impact on the continuity of the oxide overlayers and

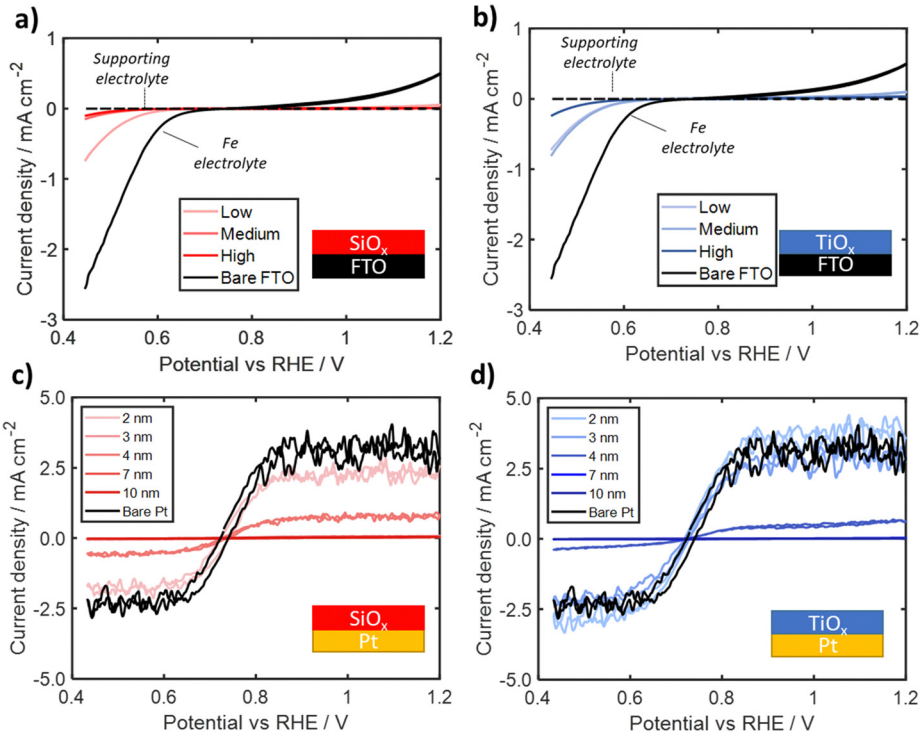

Fig. 6 Representative CV cycles of (a) SiO_x|FTO and (b) TiO_x|FTO for three different overlayer precursor concentrations (low, medium, high). Representative CV cycles for (c) SiO_x|Pt and (d) TiO_x|Pt electrodes with varied overlayer thicknesses measured with a scan rate of 10 mV s^{-1} in dearated aqueous Fe-containing electrolyte (25 mM $FeSO_4$ + 12.5 mM $Fe_2(SO_4)_3$ + 0.1 M Na_2SO_4 + 0.05 M H_2SO_4). For all CV curves, the black trace corresponds to the bare substrate without any overlayer.

more accurately determine how Fe(II)/Fe(III) redox features change with overlayer thickness, a series of electrodes were fabricated by depositing oxide overlayers on substrates based on a smooth p+Si(100) wafers. First, overlayers were deposited directly onto the as-received p+Si substrate. None of these electrodes exhibited any significant electrochemical features associated with Fe redox reactions (Fig. S25, ESI†). While this result may demonstrate that there are no Fe-redox-active sites present on either the SiO_x or TiO_x overlayers, it is possible that the presence of a 1–2 nm native silicon oxide layer present on the Si wafer could be suppressing redox signal by increasing electrical resistance between the substrate and overlayer.[65]

Finally, overlayers were deposited onto p+Si(100) wafers coated with 50 nm of Pt, which served as a proxy for Ir that is also very active towards Fe(II)/Fe(III) redox reactions. Representative CV curves recorded for overlayers with thicknesses varying between 2–10 nm are seen in Fig. 6c and d for SiO_x|Pt and TiO_x|Pt respectively. For all electrodes, CV curves display an apparent mass transport limited current densities at large overpotentials for both the FeRR and the FeOR. For the thinnest overlayers (< 4 nm), there is a decrease in the apparent limiting current for SiO_x|Pt electrodes while the limiting current for the TiO_x|Pt electrodes remain the same as the bare Pt electrode. Above this thickness threshold of ≈ 4 nm, the Fe(II)/Fe(III) redox signal for both types of oxide layers becomes similar to the background signal. Interestingly, this near complete suppression of Fe redox is different from the data in Fig. 5b and c, where appreciable FeOR and FeRR current was still observed for thicknesses up to 9 nm for both Pt|TiO_x|Pt and Pt|SiO_x|Pt in the presence of an active outer Pt layer. This suggests that the outer surfaces of both TiO_x and SiO_x may not possess high enough catalytic activity towards the Fe redox reactions, especially at larger thicknesses and moderate overpotentials. This difference in behavior may also be explained by differences in density of states at the outer surface, which would help facilitate tunneling of charge carriers through the oxide, as suggested in previous studies with tunneling TiO_2 layers.[62,66]

2.5. Species transport through silicon oxide overlayers

To further investigate the role of species transport through the overlayer to active sites at the buried interface, the Fe(II)/Fe(III) redox behavior of 40 additional MO_x|Pt thin film electrodes with varying thickness was evaluated. Apparent FeRR limiting currents, similar to Fig. 6, recorded during CV measurements in Fe-containing electrolyte were normalized by the limiting FeRR current for a bare Pt control electrode and plotted against overlayer thickness in Fig. 7. It is seen that the limiting current for SiO_x|Pt electrodes rapidly decreases with overlayer thickness for thicknesses greater than 2 nm, while significant decreases in the limiting current density of TiO_x -encapsulated electrodes are not seen until an overlayer thickness of 3–4 nm. Above these two thickness thresholds, a drastic decrease in limiting current is followed by a more gradual decline towards zero current for thicknesses greater than ≈ 5 nm.

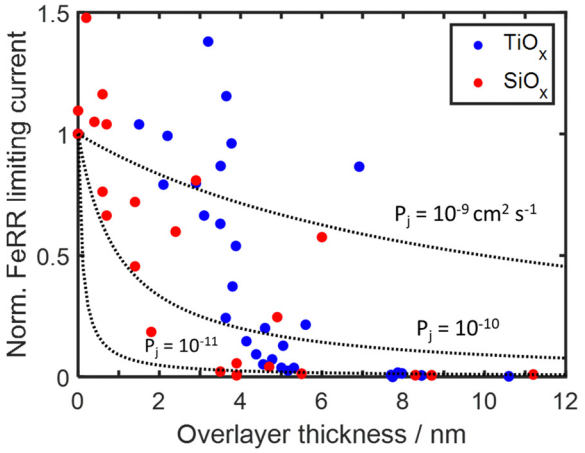

Fig. 7 Current density towards the FeRR taken over 0.45–0.5 V *vs.* RHE for 40 MO_x|Pt electrodes during CV cycling in Fe-containing electrolyte (25 mM $FeSO_4$ + 12.5 mM $Fe_2(SO_4)_3$ + 0.1 M Na_2SO_4 + 0.05 M H_2SO_4). Current densities were normalized to the limiting current density of a bare electrode and plotted as a function of overlayer thickness for both SiO_x and TiO_x overlayers. Dotted lines represent current densities predicted by the 1D diffusion model (eqn (5)) for different species permeabilities. The 1D model assumes that species transport across the diffusion boundary layer remains the same for bare Pt and MO_x|Pt electrodes.

The drastic decrease in current with increasing overlayer thickness (t_o) in Fig. 7 could be consistent with a reaction occurring on the outer surface of the overlayer (Fig. 1a) if electrical transport across the overlayer is limited by quantum mechanical tunneling through a dielectric barrier, for which tunneling probability decreases exponentially with overlayer thickness ($i \sim \exp(-t_o)$).[62] However, current is also expected to decrease with t_o for reactions occurring at the buried interface of an oxide encapsulated electrocatalyst (Fig. 1b), for which the limiting current density should vary as $i_{lim} \sim 1/t_o$. This inverse relationship between i_{lim} and t_o is seen in eqn (3), which is based on a 1-dimensional (1D) solution-diffusion model describing reactant transport by diffusion across a diffusion boundary layer and an overlayer with thickness t_o:[17,67]

$$i_{\mathrm{lim},\,j} = \frac{n_j F C_{j,b}}{\frac{1}{k_c} + \frac{t_o}{P_j}} \tag{3}$$

where C_j is the bulk concentration of species j, k_c is the mass transfer coefficient associated with the diffusion boundary layer, and P_j is the permeability of species j within the overlayer. By taking the ratio of the limiting currents between the encapsulated ($i_{lim,MOx}$) and bare electrodes ($i_{lim,bare}$), eqn (3) can be rewritten in terms of the ratio of mass transfer coefficients associated with the diffusion boundary layer (k_c) and overlayer (P_j/t_o), assuming the diffusion boundary layer is the same for both electrodes.

$$i_{\mathrm{lim,bare}} = \frac{n_j F C_{j,b}}{\frac{1}{k_c}} \tag{4}$$

$$\frac{i_{\mathrm{lim,MOx}}}{i_{\mathrm{lim,bare}}} = \frac{1}{1 + k_c \frac{t_o}{P_j}} \quad (5)$$

Eqn (5) was used to model ($i_{\mathrm{lim,MOx}}/i_{\mathrm{lim,bare}}$) for three different permeabilities spanning three orders of magnitude (10^{-9}–10^{-11} cm^2 s^{-1}), with the results shown in Fig. 7. In this analysis, k_c was kept as a constant value corresponding to that extracted from the bare Pt electrode CVs. Comparison of the modeled curves in Fig. 7 to the experimental data points shows that the 1D diffusion model may reasonably describe ($i_{\mathrm{lim,MOx}}/i_{\mathrm{lim,bare}}$) *vs.* t_o data for SiO_x|Pt electrodes for a species permeability of $\approx 1 \times 10^{-10}$ cm^2 s^{-1}. However, the scatter present in the experimental data makes it difficult to confidently state whether the 1D diffusion model gives a better fit to the data than an exponential fit associated with quantum tunneling.

While the 1D diffusion model could be a reasonable fit to the experimental data for the SiO_x|Pt electrodes, the same cannot be said for TiO_x|Pt electrodes for any assumed Fe(III) permeability. Disagreement between the shape of the modeled curves and experimental data is especially pronounced at the lowest thicknesses (< 4 nm), where the FeRR current densities of the TiO_x-encapsulated electrodes were statistically the same as bare Pt. While this thickness-independent behavior could potentially be explained by incomplete coverage of the overlayers, conformal TiO_2 overlayers made by atomic layer deposition (ALD) exhibit similar behavior over this thickness range (Fig. S26, ESI†). Overlayers fabricated by ALD are expected to be highly conformal, even for thicknesses down to 2 nm, and thus the similar FeRR behaviors suggests that the wet chemical overlayers were also conformal. Therefore, the most likely cause of the behavior for overlayer thicknesses < 4 nm is that the FeRR occurs at the outer surface over the overlayer (Fig. 1a), bypassing the need for species transport through the overlayer and resulting in similar mass transport limiting current as an unencapsulated electrode. This scenario is similar to that described by Hoffman *et al.*[14] for thin ALD TiO_2 overlayers deposited on Ir electrodes and is consistent with the thinnest TiO_x overlayers having the lowest electrical resistivity (Fig. 5d). Combining insights from Sections 2.3, 2.4, and 2.5, we conclude that active sites exist on the outer surface of the TiO_x overlayers, and that the bulk material possesses sufficiently low electronic resistivity to support meaningful electron transfer to those sites for TiO_x overlayer thicknesses < 4 nm. For t_o > 4 nm, the electrical resistance of the overlayer becomes too large, causing electron transport and/or Fe(II)/Fe(III) transport across the overlayer to become limiting.

The observations that (i) SiO_x overlayers possess very high electronic resistivity (Fig. 5), (ii) SiO_x|FTO substrates do not display any meaningful OER activity (Fig. S25 and S27, ESI†), and (iii) SiO_x|Ir electrodes exhibit similar OER performance as bare Ir electrodes (Fig. 4), suggest that the OER is occurring at the SiO_x|Ir buried interface as depicted in Fig. 1b. For this to happen, H_2O, O_2, and H^+ must be able to transport through the SiO_x overlayers with low energy penalty. Meanwhile, the high selectivity towards the OER *vs.* FeOR is likely explained by Fe(II) species being selectively blocked by a semipermeable oxide overlayer, which is consistent with the observations that little-to-no Fe(II) oxidation signal is observed for SiO_x|Ir (Fig. 4c), SiO_x|FTO (Fig. 6a), or SiO_x|Pt (Fig. 6c) electrodes. Additionally, a recent molecular dynamics study by Aydin *et al.* suggested that Fe(II) and Fe(III) transport through SiO_2 is constrained by size exclusion of the solvated ions,[40] while it is well-established that dense SiO_x overlayers can readily transport H^+ through a facilitated diffusion process involving hopping of protons along a H-bonding network within SiO_2.[58,68,69] However, some studies have reported that SiO_2[70] and MoO_x[9] overlayers can be effective at blocking O_2 transport, including a recent study from our group that reported that O_2 permeability of SiO_2 overlayers can be two orders of magnitude lower than the permeability of H^+.[58]

To better understand transport mechanism of species through SiO_x coatings, classical molecular dynamics (MD) simulations were carried out for 2 nm thick SiO_2 slabs with a well-defined pore diameter of 0.8 nm (Fig. 8a). Additional studies on nanoscopic SiO_x on platinum suggest species transport is associated with the formation of Si–O–Si ring structures[71] with diameters > 0.3 nm.[72] Previous characterization of SiO_x overlayers deposited by the UV-ozone process by ellipsometric porosimetry indicated that pores, if they exist, have average diameters that are less than 0.6 nm[6] while other studies on nanoscopic SiO_x on carbon nanotubes suggest pores are likely < 0.7 nm through BET analysis.[73] Thus, by using MD simulations to investigate species transport for a pore diameter slightly larger than 0.6 nm, this study is being conservative in

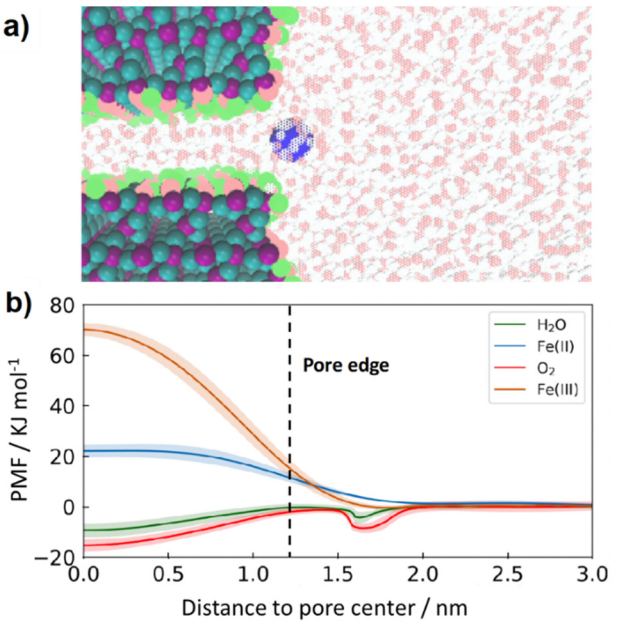

Fig. 8 (a) Representative illustration of the molecular dynamics simulation consisting of an aqueous solution phase [water (H: red, O: white), and Fe(II) (blue) ion] and a single SiO_2 (Si: purple, O:cyan) pore with a hydroxylated surface and a pore size of 0.8 nm (O: pink, H: light green) (b) potential of mean force (PMF) as a function of distance to the SiO_2 pore center for O_2, H_2O, Fe(II) and Fe(III). PMF curves for Fe(II) and Fe(III) are reproduced from ref. 40.

its assessment of whether species are likely to enter and diffuse through the overlayers.

Results of MD simulations are provided in Fig. 8b, where the potential of mean force (PMF) for H_2O, O_2, Fe(II), and Fe(III) permeants are shown as a function of their location with respect to the pore center. These results predict that transport of both O_2 (red line) and H_2O (green line) from the bulk electrolyte into a 0.8 nm pore is barrierless, meaning that there is no energy penalty for these permeants to enter the pore. This lack of energy barrier is attributed to favorable interactions between both O_2 and H_2O with the silanol groups present in the SiO_2 pore that overcome the energy penalty associated with the breaking of hydrogen bonds when entering the pore.[74] In sharp contrast, the energy barrier for Fe(II) (blue line) and Fe(III) (orange line) transport is found to be significantly higher than that of O_2 and H_2O, providing further evidence that SiO_2 overlayers promote selectivity towards the OER over the FeOR thanks to their ability to block Fe(II) from reaching buried active sites while still permitting diffusion of H_2O and O_2 into free volume elements of SiO_2 from the bulk electrolyte. The energy barriers of Fe species were due to modulation of solvation structures albeit qualitatively different between Fe(II) and Fe(III): loss of weakly bound second shell and large strain in strongly bound second shell, respectively.[40]

III. Conclusions

This study demonstrates that TiO_x- and SiO_x-encapsulated iridium electrocatalysts can significantly enhance the selectivity towards the OER over the competing Fe(II) oxidation reaction with minimal impact on the OER activity. The ability to suppress Fe(II)/Fe(III) redox reactions while permitting the OER is highly dependent on the thickness of the oxide overlayer, with SiO_x overlayers being more effective at blocking Fe(II)/Fe(III) reactions than TiO_x overlayers of the same thickness. However, Fe(II)/Fe(III) redox reactions may occur at very thin (< 4 nm) TiO_x overlayers, while comparable SiO_x overlayers show suppressed electrochemical activity. The effectiveness of SiO_x overlayers to suppress Fe(II)/Fe(III) reactions on their outer surface is explained by their large through-plane electronic resistivity, which is around one order of magnitude larger than for TiO_x. Furthermore, molecular dynamics simulations show that H_2O and O_2 species experience low energy barriers for transport through model SiO_2 nanopores–thus allowing the OER to proceed at the oxide/Ir interface—while Fe(II) and Fe(III) species transport is hindered by large energy barriers. This ability to manipulate the selectivity of OER electrocatalysts in the presence of a competing redox species through rational design of oxide overlayer properties is relevant to a number of applications, including but not limited to seawater electrolysis and Z-scheme photocatalysis. Through precise control over both charge carrier and species transport, oxide-encapsulated electrocatalysts also offer an attractive approach for designing multi-site electrocatalysts for co-optimization of selectivity and activity for more complex multi-step redox reactions.

Material and methods

Electrode fabrication

Electrodes were fabricated on either FTO glass (TEC7, 2.2 mm thick, GreatSolarCell), or monocrystalline degenerately doped p+Si(100) wafers (Prime-grade p+Si, resistivity < 0.005 Ω cm, 500–550 μm thick, WRS materials). The iridium electrodes were prepared by sputter coating a thin layer of iridium ($\sim$ 50 nm) using an EMS150T sputter coater (Electron Microscopy Sciences, Hatfield, PA, USA) onto the aforementioned FTO glass substrate. For metal|p+Si based electrodes, 50 nm of Pt was deposited at a rate of 1 Å s^{-1} with a 2 nm Ti adhesion layer (deposited at 0.5 Å s^{-1}). For the fabrication of SiO_x overlayers: low, medium and high precursor solutions of high-molecular-weight trimethyl siloxy-terminated poly(dimethylsiloxane) (PDMS) (600 000 cSt, Gelest) in toluene (1.2, 3.3, and 5.3 mg mL^{-1}) were spin-coated for 2.5 min at 4000 rpm.[28] For the fabrication of TiO_x overlayers solutions of titanium isopropoxide (TTIP) (97%, Sigma Aldrich) in anhydrous ethanol (2, 5, 10 mg mL^{-1}) were spin-coated for 1 min at 1000 rpm. The PDMS and TTIP coated electrodes were then dried in a vacuum oven (30 in Hg) at 90 °C for 1 h before undergoing treatment in the UV-ozone chamber (UVOCS, T10X10/OES) for 2 h to convert the PDMS to SiO_x and the TTIP to TiO_x. Replicate electrodes were fabricated in all cases to ensure reproducibility. A range of precursor solutions (0.5–6 mg mL^{-1} of PDMS in toluene for SiO_x or 1–6 mg mL^{-1} TTIP in ethanol for TiO_x) were prepared for varying overlayer thickness between 1–15 nm, which was measured *via* ellipsometry. Electrical contacts were attached by soldering a copper wire onto the front of the Ir electrode, or the back of the p+Si substrates using a solder temperature of 220 °C. The geometric area was defined using 3 M electroplaters tape with a circular opening of 0.25 cm^2 through which the electrode was exposed to electrolyte. To create the Pt|SiO_x|Si and Pt|TiO_x|Si electrodes 1 nm of Pt was deposited on SiO_x|Si and TiO_x|Si substrates through electron beam deposition at a rate of 0.3 Å s^{-1}.

Atomic layer deposited TiO_x overlayers were deposited in a custom deposition chamber at 150 °C using alternating cycles of titanium(IV) chloride ($TiCl_4$) and water in N_2 carrier gas. One cycle consisted of 1 s pulse of $TiCl_4$, 1 s N_2 purge, followed by 1 s pulse of H_2O and 3 s N_2 purge. Samples with various cycles were synthesized all under continuous flow conditions.

Electrode characterization

Overlayer thickness of electrodes on p+Si(100) substrates were measured using a J. A. Woollam α-SE ellipsometer. Thicknesses of the SiO_x and TiO_x overlayers were determined by fitting the raw data to Cauchy model with optical constants for SiO_2 and TiO_2. Thickness of the SiO_x and TiO_x overlayers for electrodes on the FTO substrates were estimated by measuring the thickness of the SiO_x and TiO_x overlayer on smooth Pt-coated Si substrates after undergoing identical spin-coating procedures.

X-ray photoelectron spectroscopy measurements were made with a PHI XPS system at pressures $< 2 \times 10^{-10}$ torr using a monochromatic Al Kα source (15 kV, 20 mA) and a charge

neutralizer, tilted to 54.7° relative to the detector. Multiplex spectra are shown as averages of three measurements and were fit using CasaXPS software applying Shirley's algorithm for background subtraction. Atomic ratios were calculated by normalizing the intensity of each element's atomic sensitivity factor.

Surface topography and roughness was measured using a BrukerDimension Icon atomic force microscope (AFM) in air using a ScanAsyst silicon tip on a nitride cantilever with a 2 nm nominal tip radius and a spring force constant of 0.4 N m^{-1}. Measurements were performed in peak force nanomechanical mapping mode using a scan rate of 0.22 Hz and a resonant frequency of 70 kHz.

Electrochemical measurements

All electrochemical measurements were performed in deaerated aqueous 0.1 M Na_2SO_4 (ACS reagent, ≥99.0%, anhydrous, granular, Sigma Aldrich) + 0.05 M H_2SO_4 (Certified ACS plus, Fischer Scientific) in 18 MΩ cm deionized water (Millipore, Milli-Q Direct 8) that was adjusted to pH 1.5 using concentrated sulfuric acid or sodium hydroxide. The iron-containing electrolyte was prepared identically except for the addition of 25 mM $FeSO_4{\cdot}7H_2O$ (ACS reagent, ≥99.0%, Sigma Aldrich) and 12.5 mM $Fe_2(SO4)_3{\cdot}xH_2O$ (97%, Sigma Aldrich). Measurements of pH were taken with a benchtop pH meter (Fisher Science Education, S90526), using a 3-point calibration from 1.69, 4.01, 7.00 standard buffers (Oakton). Bulk electrochemical measurements were conducted with an SP-200 BioLogic potentiostat, a commercial Ag|AgCl (sat. 3 M KCl) reference electrode (E° = 0.21 V *vs.* NHE, Hach, E21M002), a carbon rod (Saturn Industries) counter electrode and a standard glass three neck round bottom flask (Ace Glass, European flask, 250 mL). Electrolyte for all electrochemical experiments was deaerated by purging nitrogen (Airgas, 99.99% purity) for 20 min prior to experimentation. Sandwich structure experiments were completed by mounting Pt|MO_x|Pt|p+Si electrodes onto a custom designed Teflon enclosed stainless steel holder (47 mm diameter) which was directly mounted onto a rotator (MSR Rotator, Pine Research). The geometric area was defined using 3M electroplaters tape with a circular opening of 0.25 cm^2 through which the electrode was exposed to electrolyte.

Internal resistance of each electrode was measured by performing potentiometric electrochemical impedance spectroscopy (PEIS) at open circuit potential from 200 kHz–100 mHz with an amplitude of 10 mV before performing cyclic voltammetry measurements. Cyclic voltammetry measurements for Ir based electrodes were performed between potentials of 0.42 and 1.65 V *vs.* RHE with a scan rate of 20 mV s^{-1} for 5 cycles. Cyclic voltammetry measurements for p+Si and FTO based electrodes without Ir were performed between potentials of −0.1 and 1.65 V *vs.* RHE with a scan rate of 20 mV s^{-1} for 3 cycles, after initial pre-treatment scans between 0.05 and 1.15 V *vs.* RHE with a scan rate of 100 mV s^{-1} for 20 cycles. Electrochemical testing in supporting electrolyte (where applicable) was additionally completed before any Fe containing electrolyte. RDE scans were completed between potentials of 0.2 and 1.2 V *vs.* RHE with a scan rate of 20 mV s^{-1} for three different rotation rates of 50, 100, and 250 RPM.

Molecular dynamics simulations

Models of SiO_2 slit pores were created using a four-step process described in our recent study,[40] which we briefly summarize here. Starting with the α-quartz phase of SiO_2, an orthorhombic supercell with dimensions of 24.0 × 34.0 × 32.4 $Å^3$ was constructed. Several layers of the oxide were then removed to create slit pores, and surface oxygens were terminated with hydrogen atoms. An extra vacuum region was then added and filled by aqueous solutions that contain water molecules, a redox shuttle, and chloride ions for charge neutrality. For the simulations involving gas transport, either an O_2 or H_2 molecule was added to the aqueous solution. The system was equilibrated for 1 ns under the NPT ensemble at T = 298.15 K and P = 1 atm by using the Berendsen barostat.[75] To prevent rigid-body translation, silicon and oxygen atoms in the middle of the SiO_2 slab were constrained, while all other atoms were allowed to move. The Lennard-Jones (LJ) parameters for Fe(III) and Fe(II) were obtained from the literature,[76,77] and those for O_2 were also obtained from the literature.[78] Finally, the LJ parameters provided by Joseph and Aluru were used for the pore structure atoms.[79] A rigid SPCE water model was used in all simulations.[80]

After equilibrium, free energy surfaces associated with the transport of redox shuttles, water, and O_2 through SiO_2 pores were determined using well-tempered metadynamics (WT-MetaD) simulations.[81] This method involves adding Gaussian potentials to the system's free energy landscape based on predetermined collective variables. Two collective variables were selected: the center-of-mass (COM) distances between the permeant and the pore in two directions (parallel and perpendicular to the pore surface) for water and O_2. For the Fe ions, the collection variables were the COM distance between the ion and the pore and the number of water molecules in the first hydration shell of the ion. Statistics was collected for four replicas of WT-MetaD simulations, each spanning 350–450 ns. The simulations were carried out under the NVT ensemble at T = 298.15 K using the Nose–Hoover thermostat.[82] The Gaussian bias energy was deposited every 500 steps with specific heights and widths for each collection variable, as described in a recent study.[40] All simulations were performed using the LAMMPS package[83] patched with PLUMED 2.5b.[84]

Author contributions:

Conceptualization: WDHS, RSS, and DVE; formal analysis: WDHS, RSS, JJ, ZC, MX, FA, and MA; funding acquisition: DVE, and SA; investigation: WDHS, RSS, JJ, YW, ZC, MX, FA, MFCA and KEH; methodology: WDHS, RSS, ZC, MX, TAP, TO, DVE; supervision: SA, XP, DE, TAP, TO, and DVE; visualization: WDHS, RSS, ZC, JJ, and FA; writing – original draft: WDHS, RSS,

and JJ; and writing – review and editing: WDHS, RSS, JJ, ZC, MX, FA, TAP, SA, KEH, and DVE.

Conflicts of interest

There are no conflicts to declare.

Acknowledgements

The authors acknowledge funding from the Department of Energy, Office of Energy Efficiency and Renewable Energy (EERE) Hydrogen Fuel Cells Technologies Office and specifically the HydroGEN Advanced Water Splitting Materials Consortium, established as part of the Energy Materials Network under this same office (Award No. DE-EE0008838). EERE funding supported early R&D efforts including synthesis, characterization (TEM, XPS, AFM), and evaluation of the performance of oxide-encapsulated Ir electrocatalysts, in addition to molecular dynamics simulations. Nearly equal funding support was provided through Ensembles of Photosynthetic Nanoreactors (EPN), an Energy Frontier Research Center funded by the U.S. Department of Energy, Office of Science under Award Number DE-SC0023431. This second funding source supported a majority of manuscript writing efforts as well as additional experiments and data analysis related to oxide overlayer conductivity measurements, TEM characterization, XPS characterization, and stability measurements. The authors acknowledge the use of facilities and instrumentation supported by NSF through the Columbia University, Columbia Nano Initiative, and the Materials Research Science and Engineering Center DMR-2011738. The authors acknowledge the use of facilities and instrumentation at the UC Irvine Materials Research Institute (IMRI), which is supported in part by the National Science Foundation through the UC Irvine Materials Research Science and Engineering Center (DMR-2011967). Part of this work was performed under the auspices of the U.S. Department of Energy by Lawrence Livermore National Laboratory under Contract DE-AC52-07NA27344. Part of this work was authored by the National Renewable Energy Laboratory, operated by Alliance for Sustainable Energy, LLC, for the U.S. Department of Energy (DOE) under Contract No. DE-AC36-08GO28308.

References

1 Z. W. Seh, J. Kibsgaard, C. F. Dickens, I. Chorkendorff, J. K. Norskov and T. F. Jaramillo, *Science*, 2017, 355.
2 D. V. Esposito, V. Guilimondi, J. G. Vos and M. T. M. Koper, *Ultrathin Oxide Layers for Solar and Electrocatalytic Systems*, The Royal Society of Chemistry, 2022, pp. 167–209.
3 S. Takenaka, N. Susuki, H. Miyamoto, E. Tanabe, H. Matsune and M. Kishida, *Chem. Commun.*, 2010, **46**, 8950–8952.
4 S. Takenaka, H. Miyamoto, Y. Utsunomiya, H. Matsune and M. Kishida, *J. Phys. Chem. C*, 2014, **118**, 774–783.
5 N. Y. Labrador, X. X. Li, Y. K. Liu, H. Y. Tan, R. Y. Wang, J. T. Koberstein, T. P. Moffat and D. V. Esposito, *Nano Lett.*, 2016, **16**, 6452–6459.
6 N. Y. Labrador, E. L. Songcuan, C. De Silva, H. Chen, S. J. Kurdziel, R. K. Ramachandran, C. Detavernier and D. V. Esposito, *ACS Catal.*, 2018, **8**, 1767–1778.
7 J. E. Robinson, N. Y. Labrador, H. Chen, B. E. Sartor and D. V. Esposito, *ACS Catal.*, 2018, **8**, 11423–11434.
8 R. A. Krivina, M. Zlatar, T. N. Stovall, G. A. Lindquist, D. Escalera-López, A. K. Cook, J. E. Hutchison, S. Cherevko and S. W. Boettcher, *ACS Catal.*, 2023, **13**, 902–915.
9 A. T. Garcia-Esparza, T. Shinagawa, S. Ould-Chikh, M. Qureshi, X. Peng, N. Wei, D. H. Anjum, A. Clo, T. C. Weng, D. Nordlund, D. Sokaras, J. Kubota, K. Domen and K. Takanabe, *Angew. Chem., Int. Ed.*, 2017, **56**, 5780–5784.
10 K. Maeda, K. Teramura, D. Lu, N. Saito, Y. Inoue and K. Domen, *Angew. Chem., Int. Ed.*, 2006, **45**, 7806–7809, DOI: **10.18434/T4T88K**.
11 A. A. Bhardwaj, J. G. Vos, M. E. S. Beatty, A. F. Baxter, M. T. M. Koper, N. Y. Yip and D. V. Esposito, *ACS Catal.*, 2021, **11**, 1316–1330.
12 J. G. Vos and M. T. M. Koper, *J. Electroanal. Chem.*, 2018, **819**, 260–268.
13 J. G. Vos, T. A. Wezendonk, A. W. Jeremiasse and M. T. M. Koper, *J. Am. Chem. Soc.*, 2018, **140**, 10270–10281.
14 C. E. Finke, S. T. Omelchenko, J. T. Jasper, M. F. Lichterman, C. G. Read, S. Lewis and M. R. Hoffmann, *Energy Environ. Sci.*, 2019, **12**, 358–365.
15 B. Hou, L. Shen, H. Shi, J. Chen, B. Zhao, K. Li, Y. Wang, G. Shen, M.-A. Ha, F. Liu, A. N. Alexandrova, W. H. Hung, J. Dawlaty, P. Christopher and S. B. Cronin, *ACS Appl. Mater. Interfaces*, 2019, **11**, 10351–10355.
16 G. Lu, A. Linsebigler and J. T. Yates, Jr., *J. Phys. Chem.*, 1994, **98**, 11733–11738.
17 D. V. Esposito, V. Guilimondi, J. G. Vos and M. T. M. Koper, in *Energy and Environment Series*, ed. H. Frei and D. Esposito, Royal Society of Chemistry, Cambridge, 2022, pp. 167–209.
18 T. Kotani, K. Ogawa, H. Suzuki, K. Kato, O. Tomita, A. Yamakata and R. Abe, *EES Catal.*, 2023, **1**, 255–262.
19 L. An, C. Wei, M. Lu, H. Liu, Y. Chen, G. G. Scherer, A. C. Fisher, P. Xi, Z. J. Xu and C. H. Yan, *Adv. Mater.*, 2021, **33**, 2006328.
20 J. Guo, Y. Zheng, Z. Hu, C. Zheng, J. Mao, K. Du, M. Jaroniec, S.-Z. Qiao and T. Ling, *Nat. Energy*, 2023, **8**, 264–272.
21 K. Obata and K. Takanabe, *Angew. Chem.*, 2018, **130**, 1632–1636.
22 C. L. Mirley and J. T. Koberstein, *Langmuir*, 1995, **11**, 1049–1052.
23 J. M. Casas, G. Crisóstomo and L. Cifuentes, *Hydrometallurgy*, 2005, **80**, 254–264.
24 T. V. Sawant and J. R. McKone, *ACS Appl. Energy Mater.*, 2018, **1**, 4743–4753.
25 L. W. Hruska and R. F. Savinell, *J. Electrochem. Soc.*, 1981, **128**, 18–25.
26 R. Bala Chandran, S. Breen, Y. Shao, S. Ardo and A. Z. Weber, *Energy Environ. Sci.*, 2018, **11**, 115–135.

27 D. M. Fabian, S. Hu, N. Singh, F. A. Houle, T. Hisatomi, K. Domen, F. E. Osterloh and S. Ardo, *Energy Environ. Sci.*, 2015, **8**, 2825–2850.
28 M. E. S. Beatty, H. Chen, N. Y. Labrador, B. J. Lee and D. V. Esposito, *J. Mater. Chem. A*, 2018, **6**, 22287–22300.
29 S. J. Freakley, J. Ruiz-Esquius and D. J. Morgan, *Surf. Interface Anal.*, 2017, **49**, 794–799.
30 NIST X-ray Photoelectron Spectroscopy Database, NIST Standard Reference Database Number 20, National Institute of Standards and Technology, Gaithersburg MD, 20899 (2000), DOI: 10.18434/T4T88K, (retrieved 11/2023).
31 Y. Mei, S. Guo, Y. Jiang, F. Li, Y. Li and X. Hu, *Electrochim. Acta*, 2020, **344**, 136149.
32 J. F. Moulder and J. Chastain, Handbook of X-ray Photoelectron Spectroscopy: A Reference Book of Standard Spectra for Identification and Interpretation of XPS Data, *Physical Electronics Division*, PerkinElmer Corporation, 1992.
33 M. C. Biesinger, L. W. M. Lau, A. R. Gerson and R. S. C. Smart, *Appl. Surf. Sci.*, 2010, **257**, 887–898.
34 E. McCafferty and J. P. Wightman, *Surf. Interface Anal.*, 1998, **26**, 549–564.
35 C. D. Wagner, D. E. Passoja, H. F. Hillery, T. G. Kinisky, H. A. Six, W. T. Jansen and J. A. Taylor, *J. Vac. Sci. Technol.*, 1982, **21**, 933–944.
36 T. Reier, M. Oezaslan and P. Strasser, *ACS Catal.*, 2012, **2**, 1765–1772.
37 T. Shinagawa, A. T. Garcia-Esparza and K. Takanabe, *Sci. Rep.*, 2015, **5**, 13801.
38 Y. Zhao, N. M. Vargas-Barbosa, E. A. Hernandez-Pagan and T. E. Mallouk, *Small*, 2011, **7**, 2087–2093.
39 M. Bernt, A. Siebel and H. A. Gasteiger, *J. Electrochem. Soc.*, 2018, **165**, F305.
40 F. Aydin, M. F. C. Andrade, R. S. Stinson, A. Zagalskaya, D. Schwalbe-Koda, Z. Chen, S. Sharma, A. Maiti, D. V. Esposito, S. Ardo, T. A. Pham and T. Ogitsu, *ACS Appl. Mater. Interfaces*, 2023, **15**, 17814–17824.
41 Y. Qi, S. Chen, J. Cui, Z. Wang, F. Zhang and C. Li, *Appl. Catal., B*, 2018, **224**, 579–585.
42 S. S. Chen, J. J. M. Vequizo, Z. H. Pan, T. Hisatomi, M. Nakabayashi, L. H. Lin, Z. Wang, K. Kato, A. Yamakata, N. Shibata, T. Takata, T. Yamada and K. Domen, *J. Am. Chem. Soc.*, 2021, **143**, 10633–10641.
43 A. G. Scheuermann, K. W. Kemp, K. Tang, D. Q. Lu, P. F. Satterthwaite, T. Ito, C. E. D. Chidsey and P. C. McIntyre, *Energy Environ. Sci.*, 2016, **9**, 504–516.
44 A. F. Gil, L. Galicia and I. González, *J. Electroanal. Chem.*, 1996, **417**, 129–134.
45 A. Daniyan, L. Umoru, A. Fasasi, J. Borode, K. Oluwasegun and S. Olusunle, *J. Miner. Mater. Charact. Eng.*, 2014, **2**, 15–20.
46 S. Amirtharajan, P. Jeyaprakash, J. Natarajan and P. Natarajan, *Appl. Nanosci.*, 2016, **6**, 591–598.
47 F. Zeribi, A. Attaf, A. Derbali, H. Saidi, L. Benmebrouk, M. S. Aida, M. Dahnoun, R. Nouadji and H. Ezzaouia, *ECS J. Solid State Sci. Technol.*, 2022, **11**, 023003.
48 A. Yildiz, S. B. Lisesivdin, M. Kasap and D. Mardare, *J. Non-Cryst. Solids*, 2008, **354**, 4944–4947.
49 H. Bartzsch, D. Glöß, B. Böcher, P. Frach and K. Goedicke, *Surf. Coat. Technol.*, 2003, **174–175**, 774–778.
50 D. Wang, J. Liu, Z. Lv, H. Tao, Y. Cui, H. Wang, S. Liu, C. Liu, N. Wang, W. Jiang, W. Chai and W. Ding, *Mater. Lett.*, 2018, **211**, 277–280.
51 Q. Wang, Z. Liu, Z. Liu, Z. Li, J. Yin, H. Wang, W. Jiang, S. Liu, Y. Cui, W. Ding and C. Dong, *Appl. Surf. Sci.*, 2023, **636**, 157791.
52 W. R. Ayles, *et al.*, in *Engineered materials handbook*, ed. M. M. Gauthier, ASM International, Amsterdam, Desk edn, 1995, ch. 30.
53 H. E. Wenden, *Am. Mineral.*, 1957, **42**, 859–888.
54 A. G. Scheuermann, J. D. Prange, M. Gunji, C. E. D. Chidsey and P. C. McIntyre, *Energy Environ. Sci.*, 2013, **6**, 2487.
55 E. Kumi-Barimah, R. Penhale-Jones, A. Salimian, H. Upadhyaya, A. Hasnath and G. Jose, *Sci. Rep.*, 2020, **10**, 10144.
56 H. Tang, K. Prasad, R. Sanjinès, P. E. Schmid and F. Lévy, *J. Appl. Phys.*, 1994, **75**, 2042–2047.
57 Y. Katsuta, R. Akahane and K. Yahagi, *Jpn. J. Appl. Phys.*, 1971, **10**, 976.
58 M. E. S. Beatty, E. I. Gillette, A. T. Haley and D. V. Esposito, *ACS Appl. Energy Mater.*, 2020, **3**, 12338–12350.
59 J. Nowotny, T. Bak, M. K. Nowotny and L. R. Sheppard, *Int. J. Hydrogen Energy*, 2007, **32**, 2630–2643.
60 X. Liu, H. Xu, L. R. Grabstanowicz, S. Gao, Z. Lou, W. Wang, B. Huang, Y. Dai and T. Xu, *Catal. Today*, 2014, **225**, 80–89.
61 A. J. Bard, L. R. Faulkner and H. S. White, *Microscopic Theories of Charge Transfer*, Wiley, 2022, vol. 3, pp. 142–168.
62 C. M. Hill, J. Kim and A. J. Bard, *J. Am. Chem. Soc.*, 2015, **137**, 11321–11326.
63 Y. W. Chen, J. D. Prange, S. Dühnen, Y. Park, M. Gunji, C. E. D. Chidsey and P. C. McIntyre, *Nat. Mater.*, 2011, **10**, 539–544.
64 A. Korjenic and K. S. Raja, *J. Electrochem. Soc.*, 2019, **166**, C169–C184.
65 M. Morita, T. Ohmi, E. Hasegawa, M. Kawakami and K. Suma, *Appl. Phys. Lett.*, 1989, **55**, 562–564.
66 C. M. Hill, J. Kim, N. Bodappa and A. J. Bard, *J. Am. Chem. Soc.*, 2017, **139**, 6114–6119.
67 D. V. Esposito, *ACS Catal.*, 2018, **8**, 457–465.
68 J. Godet and A. Pasquarello, *Phys. Rev. Lett.*, 2006, **97**, 155901.
69 H. A. Kurtz and S. P. Karna, *IEEE Trans. Nucl. Sci.*, 1999, **46**, 1574–1577.
70 W. J. Jo, G. Katsoukis and H. Frei, *Adv. Funct. Mater.*, 2020, **30**, 1909262.
71 J. A. Bau and K. Takanabe, *ACS Catal.*, 2017, **7**, 7931–7940.
72 S. T. Oyama, D. Lee, P. Hacarlioglu and R. F. Saraf, *J. Membr. Sci.*, 2004, **244**, 45–53.
73 S. Takenaka, T. Miyazaki, H. Matsune and M. Kishida, *Catal. Sci. Technol.*, 2015, **5**, 1133–1142.
74 A. M. Schrader, J. I. Monroe, R. Sheil, H. A. Dobbs, T. J. Keller, Y. Li, S. Jain, M. S. Shell, J. N. Israelachvili and S. Han, *Proc. Natl. Acad. Sci. U. S. A.*, 2018, **115**, 2890–2895.

75 H. J. C. Berendsen, J. P. M. Postma, W. F. van Gunsteren, A. DiNola and J. R. Haak, *J. Chem. Phys.*, 1984, **81**, 3684–3690.
76 P. Li, L. F. Song and K. M. Merz, Jr., *J. Phys. Chem. B*, 2015, **119**, 883–895.
77 P. Li, B. P. Roberts, D. K. Chakravorty and K. M. Merz, Jr., *J. Chem. Theory Comput.*, 2013, **9**, 2733–2748.
78 S. Wang, K. Hou and H. Heinz, *J. Chem. Theory Comput.*, 2021, **17**, 5198–5213.
79 S. Joseph and N. R. Aluru, *Langmuir*, 2006, **22**, 9041–9051.
80 H. J. C. Berendsen, J. R. Grigera and T. P. Straatsma, *J. Phys. Chem.*, 1987, **91**, 6269–6271.
81 A. Barducci, G. Bussi and M. Parrinello, *Phys. Rev. Lett.*, 2008, **100**, 020603.
82 S. Nosé, *J. Chem. Phys.*, 1984, **81**, 511–519.
83 S. Plimpton, *J. Comput. Phys.*, 1995, **117**, 1–19.
84 G. A. Tribello, M. Bonomi, D. Branduardi, C. Camilloni and G. Bussi, *Comput. Phys. Commun.*, 2014, **185**, 604–613.